Applied Catalysis B: Environmental 325 (2023) 122324

Contents lists available at ScienceDirect

Applied Catalysis B: Environmental

journal homepage: www.elsevier.com/locate/apcatb

Refined alteration of active sites via O modification on CoP/Co_2P@Carbon hetero-structural catalyst for hydrogen generation

Huanhuan Zhang [a,c], Yanyan Liu [b,c,d,*], Limin Zhou [c], Huijuan Wei [c], Hao Wen [c], Zhenggang Wang [c], Xinzheng Yue [c], Xianli Wu [c], Yulong Zhang [a], Baozhong Liu [a,e], Yanping Fan [a,**], Huaqiang Cao [f], Jianchun Jiang [d], Baojun Li [a,c,f,***]

[a] College of Chemistry and Chemical Engineering, Henan Polytechnic University, 2001 Century Avenue, Jiaozuo 454000, PR China
[b] College of Science, Henan Agricultural University, 95 Wenhua Road, Zhengzhou 450002, PR China
[c] Research Center of Green Catalysis, College of Chemistry, Zhengzhou University, 100 Science Road, Zhengzhou 450001, PR China
[d] Institute of Chemical Industry of Forest Products, CAF, National Engineering Lab for Biomass Chemical Utilization, Key and Open Lab on Forest Chemical Engineering, SFA, 16 Suojinwucun, Nanjing 210042, PR China
[e] Henan Key Laboratory of Coal Green Conversion, Henan Polytechnic University, Jiaozuo, Henan 454003, PR China
[f] Department of Chemistry, Tsinghua University, Beijing 100084, PR China

ARTICLE INFO

Keywords:
Borohydride hydrolysis
Oxygen modification
Bimolecular activation
Cobalt-based catalysts
Heterostructure

ABSTRACT

Elucidating the relationship between heterostructure and catalytic activity is scientifically significant for water-related dissociation reactions. Herein, oxygen (O) modified CoP/Co_2P@carbon heterostructure (O-(CoP/Co_2P)@SC) is deliberately designed through controlled O modification and Local P-inducing Strategy. The optimal catalyst presents potent catalytic activity (turnover frequency of 35 min^{-1}) and the stability without abominable decrease even after long-time usage. The prominent catalytic activity stems from the successful construction and refined alteration of active sites (Co atoms in form of Co-P and Co-O). Combining experimental results and density functional theory simulations, the activation energies and reaction dissociation energies of reactants (NH_3BH_3 and H_2O) are altered, thus to optimize the catalytic kinetics of NH_3BH_3 hydrolysis (active Co nearby Co-O activates H_2O and active Co nearby Co-P activates NH_3BH_3). This O modification strategy brings new inspiration for boosting catalytic activity of transition metal phosphides

1. Introduction

Hydrogen, as a clean energy carrier due to its higher energy density and the delightful advantage of being contamination-free after combustion, is considered as a promising candidate for the sustainable development [1,2]. Unfortunately, challenges such as secure storage and transport still exist in current hydrogen economy [3,4]. Therefore, the development of valid hydrogen storage materials is paramount for facilitating the high-efficient utilization of hydrogen energy [5]. Ammonia borane (NH_3BH_3) [6], sodium borohydride ($NaBH_4$) [7], hydrazine hydrate ($N_2H_4{\cdot}H_2O$) [8], and formic acid (HCOOH) [9] are commonly used chemical hydrogen storage materials. Borohydrides (NH_3BH_3, $NaBH_4$) as safe and efficient solid-state hydrogen storage materials are vital for the development of hydrogen energy [7,10]. Specifically, NH_3BH_3 features the attractive advantages such as high hydrogen content, low molecular weight, long-term stability, non-toxicity and holds the promising in hydrogen generation [11]. The formula of the hydrolysis of NH_3BH_3 is conveyed as follows:

$$NH_3BH_3 + 2H_2O \rightarrow NH_4BO_2 + 3H_2 \quad (1)$$

The release of hydrogen during the hydrolysis of NH_3BH_3 is proceeded under an appropriate catalyst [12]. Noble metals are powerful contenders in significantly reducing the reaction activation barriers between NH_3BH_3 and H_2O molecules during catalytic reaction [13,14]. Low abundance and prohibitive price seriously hamper their widespread utilization. Thus, excavating catalysts with low cost and high-efficiency activity is necessary for the development of sustainable energy. Co/Ni as transition metal holds the potential for the construction of active sites

* Corresponding author at: College of Science, Henan Agricultural University, 95 Wenhua Road, Zhengzhou 450002, PR China.
** Corresponding author.
*** Corresponding author at: College of Chemistry and Chemical Engineering, Henan Polytechnic University, 2001 Century Avenue, Jiaozuo 454000, PR China.
E-mail addresses: lyylhs180208@163.com (Y. Liu), fanyanping@hpu.edu.cn (Y. Fan), lbjfcl@zzu.edu.cn (B. Li).

https://doi.org/10.1016/j.apcatb.2022.122324
Received 13 September 2022; Received in revised form 20 December 2022; Accepted 22 December 2022
Available online 23 December 2022

for reinforcing the catalytic activity [15,16]. The strong reducibility of low valent B element and active H species generated during reaction lead to severe fading of catalytic activity. Moreover, long-standing and critical issue such as poor catalytic performance and unclear catalytic mechanism exist in hydrolysis system. Therefore, it is essential to create efficient active sites for the improvement of catalytic performance.

Ingenious design strategy of active sites in catalysts is central to optimizing the chemisorption ability of catalysts due to the adjustment of electron distribution. Transition metal phosphides (TMPs) as a kind of active materials have been widely employed in energy storage and catalysis fields due to their interesting advantages, such as abundant active sites, unique physicochemical properties, and adjustable component structure, etc. [17,18]. TMPs have metal-like features due to the generated metal-phosphorus (M-P) bond, M-M bond and P-P bond in TMPs. The introduction of phosphorus element into metal-based catalysts adjusts the chemical coordination environment of catalysts and further improves the catalytic performance [19,20]. Co-doped Ni_2P regulates the electronic structure of targeted catalyst, decreases the reaction barriers of reactants and thus enhances the hydrolysis of NH_3BH_3 [21]. The lattice stress releases caused by the substitution of phosphorus atoms results in the easy agglomeration of TMPs [22,23]. And this phenomenon damages the primary structure composition and reduces the catalytic performance [24,25]. The support has the ability to disperse metal species and naturally form the metal-support interface. It is significant for researching the relationship of metal-support interactions to further improve the catalytic performance of active components.

Carbon or silica (SiO_2) as a support has the ability to prevent the sintering and carbon collapse of metal nanoparticles due to the spatial limiting effect under the reaction conditions [26,27]. Supports can disperse the active components and maintain their stability, thus heightening the catalytic performance of catalysts in heterogeneous catalysis [28,29]. Interestingly, the construction of active sites in transition metal on support via phosphorous atom regulation is vital in investigating the correlation between active sites and catalytic performance. Heteroatom modification has the ability to further boost the catalytic activity of TMPs via the electronic regulation of the catalytically active sites at the atomic level [30]. The lattice distortion and distribution of electron density caused by the modification of different heteroatom into TMPs are responsible for the improvement of the intrinsic catalytic activity. Reports confirm that the introduction of hydrophilic oxygen into TMPs regulates the charge distribution of metal, changes the coordination environment of the central atom, thus boosting the catalytic activity of hydrogen generation [31,32]. The introduction of heteroatom oxygen element into catalyst enhances the synergy effect between CoP_2 and Pd NPs, thus facilitating the catalytic activity of hydrogen generation [33]. Therefore, to further elaborately construct active sites in TMPs via O modification and improve the chemical environment and electronic structure regulation of catalysts is crucial to enhance catalytic activity.

Collectively, the investigation of the refined alteration of active sites in CoP/Co_2P@carbon heterostructure via O modification is realized to boost the catalytic activity for efficient NH_3BH_3 hydrolysis (turnover frequency, *TOF*=35 min^{-1}). Local P-inducing Strategy (*LPiS*) is responsible for the formation of the CoP/Co_2P heterostructure. The appropriate O modification into CoP/Co_2P heterostructure promotes the catalytic activity due to the regulation of electronic structure in active sites. This joint regulation of O and P atom modification strategy modulates the coordination environment of metal Co active sites. Sequentially, the adjustment of the active sites boosts the catalytic hydrogen generation. This discovery broadens the research of metal phosphides in the construction of active sites in energy-related catalytic reactions.

2. Experimental section

2.1. Preparation of catalysts

2.1.1. Synthesis of Co-MOF@SiO_2@RF

Co-MOF was pre-fabricated according to the literature without centrifugation [34]. Co-MOF solution was stirred for 30 min along with ultrasonic for 30 min and repeated for 2 times. Subsequently, H_2O (16 mL) and absolute ethyl alcohol (4 mL) solution consisting of tetraethyl orthosilicate (TEOS, 0.08 mL) was added into the above Co-MOF solution. The Co-MOF@SiO_2 was harvested with a continuous stir for 8 h. Then, resorcinol (0.17 g) and ethylene diamine (0.17 mL) were mixed into water-ethanol solution (54 mL: 26 mL) with a stir for 30 min at 30 °C. Then formaldehyde (0.26 mL) solution was poured into the above-mentioned solution along with another 30 min and formed resorcinol formaldehyde (RF). Co-MOF@SiO_2 was joined in the RF solution with a continuous stir treatment for 48 h. Finally, the Co-MOF@SiO_2@RF precursor was collected after drying in the oven.

2.1.2. Synthesis of Co@SC, and CoO_x@SC

Co@SC (SC: refers to SiO_2@Carbon) was obtained from Co-MOF@SiO_2@RF after annealing at 700 °C for 2 h in an inert atmosphere (heating rate: 3 °C min^{-1}). The different annealing temperatures of 600 °C and 800 °C were also operated and named Co@SC-600, Co@SC-800, respectively. The control oxidation in air (200 °C for 22 h) for the above catalysts was conducted and formed CoO_x@SC, CoO_x@SC-600, CoO_x@SC-800 and other contrastive materials. In addition, the catalysts treated at different oxidation temperatures (fixed oxidation time: 22 h, oxidation temperature: 100 °C and 300 °C) and different oxidation times (fixed oxidation temperature: 200 °C, oxidation time: 12 h and 32 h) were also synthesized to further accounting for the role of O element in the process of hydrogen generation.

2.1.3. Synthesis of O-(CoP/Co_2P)@SC

Some mass of sodium hypophosphite (NaH_2PO_2) and catalysts of CoO_x@SC, CoO_x@SC-600 and CoO_x@SC-800 and other contrastive materials (mass ratio of NaH_2PO_2 and catalysts: 10/1) were put on two sides of the tube furnace, respectively. Finally, O-(CoP/Co_2P)@SC, O-(CoP/Co_2P)@SC-600, O-(CoP/Co_2P)@SC-800 and other contrastive materials were obtained after the treatment in an Argon atmosphere (heating temperature and time: 300 °C, 2 h; heating rate: 3 °C min^{-1}). Moreover, the catalysts treated at different P-inducing temperatures (fixed P-inducing time: 2 h, P-inducing temperature: 200 °C and 400 °C) and different P-inducing times (fixed P-inducing temperature: 300 °C, P-inducing time: 30 min, 60 min and 3 h) were also fabricated to deduce the effect of *LPiS* on the catalytic activity for hydrogen generation.

2.2. Hydrolysis of NH_3BH_3 and $NaBH_4$

The hydrolysis of NH_3BH_3 and $NaBH_4$ was operated via a water-displacement method. In detail, certain amounts of as-prepared catalyst were added into a round-bottom flask. Subsequently, a solution of NH_3BH_3 was poured into the flask. The generated hydrogen was collected through water-displacement method. The detailed information was proffered in Supporting Information.

2.3. Characterization

Many technologies were used to analyze the synthesized catalysts. X-ray diffraction (XRD) was conducted to analyze the phase composition of various catalysts. Scanning electron microscope (SEM) and transmission electron microscope (TEM) were operated to observe the morphologies of various catalysts. X-ray photoelectron spectroscopy (XPS) was conducted to reveal the characteristic surface elemental composition and electronic states of the catalysts. Raman spectra were implemented to certify the structural defect degree in catalysts. Inductively

coupled plasma optical emission spectrometry (ICP-OES) was applied to calculate the contents of active cobalt element in catalysts. The types and other information are conveyed in the Supporting Information.

2.4. Computational details

To further illustrate the enhanced effect of O modification on CoP/Co_2P heterostructure. The first-principles were employed to perform all Spin-polarization density functional theory (DFT) calculations with the Vienna Ab-initio Simulation Package (VASP), within the generalized gradient approximation (GGA) using the Perdew-Burke-Ernzerhof (PBE) functional. The projected augmented wave (PAW) potentials were chosen to describe the ionic cores and take valence electrons into account using a plane wave basis set with a kinetic energy cutoff of 500 eV. Partial occupancies of the Kohn−Sham orbitals were allowed using the Gaussian smearing method and a width of 0.05 eV. The electronic energy was considered self-consistent when the energy change was smaller than 10^{-4} eV. A geometry optimization was considered convergent when the energy change was smaller than 0.04 eV Å^{-1}. In the structure of this calculation, the U correction is used for Co atoms and set as 4.69 eV. The vacuum spacing in a direction perpendicular to the plane of the structure is 20 Å for the surfaces. The Brillouin zone integration is performed using 2 × 2 × 1 Monkhorst-Pack k-point sampling for the structure.

Additionally, the supercell optimization toward CoP and Co_2P was conducted to obtain a matching lattice parameter. Based on this, the operation to construct the heterostructure was carried out. Finally, the stable structure of the heterostructure was harvested through the operation of structural optimization. Illustratively, the exposed stable surface was selected during the process of calculation and all the constructed structures were stable. The detailed information is as follows, the equilibrium lattice constants of CoP unit cell were optimized to be a= 3.261 Å, b= 5.072 Å, c= 5.557 Å. Then the CoP unit cell was used to construct a CoP (012) surface supercell model. For the surface modification by oxygen, O is randomly doped on the surface of CoP and formed the O-CoP structures. And Co_2P (101) surface was established from the Co_2P structures. The Co_2P/O-CoP or Co_2P/CoP interface structures were established with the Co_2P or O-CoP surface or CoP surface with lattice parameters of a= 17.131 Å, b= 16.015 Å, c= 19.883 Å. The two atomic layers of bottom were fixed while the two atomic layers of top were allowed to relax during the process of the DFT calculation. Finally, the adsorption energies (E_{ads}) were calculated as E_{ads}=$E_{ad/sub}$-E_{ad}-E_{sub}, where $E_{ad/sub}$, E_{ad}, and E_{sub} are the total energies of the optimized adsorbate/substrate system, the adsorbate in the structure, and the clean substrate, respectively. The Gibbs free energy was calculated using the equation:

$$G=E_{ads}+ZPE-TS \quad (2)$$

where G represents the Gibbs free energy, E_{ads} refers to the total energy obtained by structural optimization through DFT, *ZPE* and *TS* are the zero point energy and entropic contributions achieved via calculating the vibration frequencies of adsorption state by DFT. In detail, for the decomposition of H_2O and NH_3BH_3, the transition state of an elementary reaction step was located by the nudged elastic band (NEB) method. In the NEB method, the path between the reactants and products was discretized into a series of four structural images. The intermediate images were relaxed until the perpendicular forces were smaller than 0.05 eV/Å. The energies (ΔG) of different intermediates are defined as ΔG= G_i-$G_{reactant}$ (G_i is the energy of intermediates, $G_{reactant}$ is the total energy of the reactants).

3. Results and discussion

3.1. Characterization of catalyst structure

The fabrication procedure of O-(CoP/Co_2P)@SC is shown in Fig. 1a. Firstly, hydrothermal treatment is applied to synthesize Co-MOF. TEOS solution is added into the Co-MOF solution. Explanatorily, SiO_2 formed by TEOS hydrolysis provides a passivation for Co-MOF and then Co-MOF@SiO_2 is successfully obtained. The introduction of TEOS prevents the growth and agglomeration of Co-MOF. Sequentially, Co-MOF@-SiO_2@RF is achieved through the composition of Co-MOF@SiO_2 and RF resin. Then Co@SC is subsequently obtained through an annealing of Co-MOF@SiO_2@RF. Noteworthily, the O element is introduced into Co@SC following control oxidation in air to change its electronic structure. Finally, the O modified hetero-structural catalyst consisting of CoP and Co_2P is harvested treated with CoO_x@SC by *LPiS*. The interfacial active sites compose of Co-O and Co-P derived from the refined alteration via O modification on CoP/Co_2P heterostructure is responsible for the exceptional catalytic activity. Experimentally, the results of catalytic activity during NH_3BH_3 hydrolysis demonstrate that the enhanced effect of O modification and *LPiS* are major regulators for targeted catalyst in boosting catalytic activity (Fig. 1b).

XRD patterns were used to examine the phase composition of various catalysts. The XRD patterns of Co@SC, CoO_x@SC, and O-(CoP/Co_2P) @SC treated at 700 °C are shown in Fig. 2a. The characteristic peaks at 44.2°, 51.5°, and 75.8° are matched to (111), (200), and (220) planes of Co, respectively (JCPDS Card No. 15–0806). The peaks at 36.8°, 59.3°, and 65.2° are correlated to (311), (511) and (440) planes of Co_3O_4, respectively (JCPDS Card No. 42–1467). The peaks of 48.4°, 52.3°, and 56.3° are detected on catalyst and correspond to (202), (103), and (212) lattice facets of CoP, respectively (JCPDS Card No. 89–2747). The peaks at 40.9° (201) and 44.1° (130) are assigned to Co_2P, respectively (JCPDS Card No. 32–0306). The XRD results confirm the successful construction of CoP and Co_2P heterostructure. Additionally, the peak positions of O-(CoP/Co_2P)@SC-600 and O-(CoP/Co_2P)@SC-800 have a consistency with O-(CoP/Co_2P)@SC (Fig. S1a, S1b). Furthermore, the XRD pattern of Co-P@SC without any oxidation treatment is provided. The peak at 44.1° is assigned to the (130) plane of Co_2P (JCPDS Card No. 32–0306). The discernible peaks of CoP species are detected at the positions of 36.3° (111), 46.2° (112), 48.1° (211), 52.3° (103), 56.4° (212) and 75.9° (303) (JCPDS Card No. 89–2747) (Fig. S1c). The above-mentioned results certify that *LPiS* plays a key role in the formation of CoP and Co_2P. Furthermore, XPS spectrum of P 2p in O-(CoP/Co_2P)@SC is fitted into three peaks (Fig. 2b), the peaks observed at 129.9 and 130.9 eV have perfect ascription to the P $2p_{3/2}$ and P $2p_{1/2}$ in CoP, respectively. The peak of 134.2 eV is attributed to $CoPO_x$ species formed by the surface oxidation of CoP [35–37]. These analyses demonstrate the successful introduction of P element. Fig. 2c is the optimized structure models of the CoP/Co_2P and O-(CoP/Co_2P). TEM was employed to unearth the morphologies of catalysts. In Fig. 2d-f, the TEM images convey that the obtained hybrid CoO_x@SC presents a spherical structure with abundant nanoparticles and the single sphere is approximately 500 nm. The SEM and TEM images uncover that O-(CoP/Co_2P)@SC has the similar morphological feature of CoO_x@SC (Fig. 2g-l). Moreover, the HRTEM image accurately validates the construction of heterostructure (Fig. 2m). Namely, the lattice spacings of 0.188 and 0.221 nm are indexed to the (211) and (121) planes of CoP and Co_2P, respectively. The above results have an accordance with the results of XRD in Fig. 2a. The accumulating circumstantial evidences define that heterostructure is successfully designed. Additionally, the uniform distribution of P, Co, and O elements on the surface of catalyst is certified by EDX-STEM elemental mapping images (Fig. 2n).

XPS technology was implemented to accurately interpret the chemical state in various catalysts. As demonstrated in Fig. 3a, the elements of P, Co, O, N, C and Si in O-(CoP/Co_2P)@SC are uncovered. In the Co 2p spectrum of O-(CoP/Co_2P)@SC, the binding energies (BEs) of Co $2p_{3/2}$

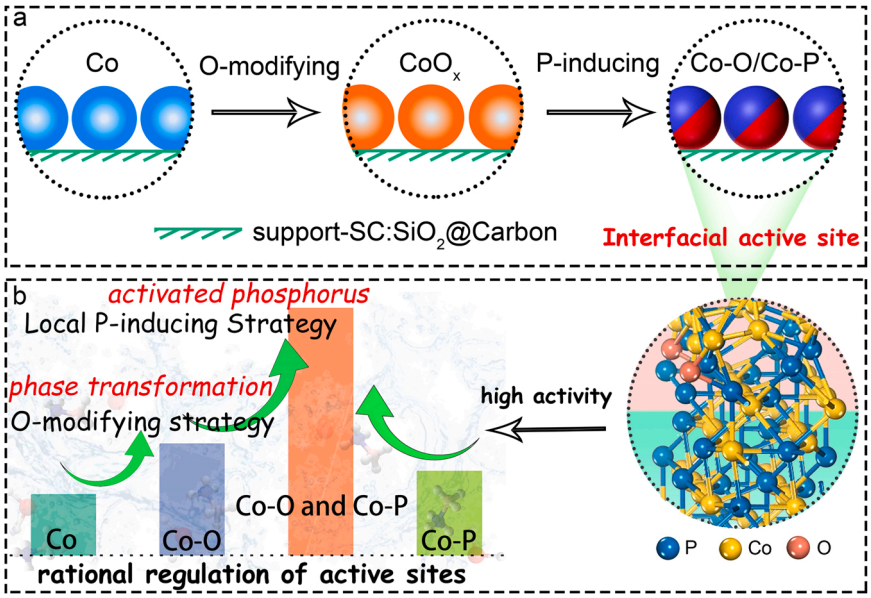

Fig. 1. (a) Simplified diagram of O-(CoP/Co_2P)@SC. (b) Refined alteration of active sites via O modifying on CoP/Co_2P heterostructure and the corresponding enhanced effect for catalytic hydrogen generation of NH_3BH_3 hydrolysis.

located at 778.8 (Co species in Co_xP), 782.2 (Co species in $CoPO_x$), and 786.1 eV (satellite peak) are observed (Fig. 3b) [38–40]. The BEs of Co $2p_{1/2}$ (793.7, 798.3, and 803.9 eV) in O-(CoP/Co_2P)@SC is similar to those of Co $2p_{3/2}$ (Fig. 3b) [35,41]. The $CoPO_x$ species exist on the surface of catalyst. Illustratively, the XRD pattern of O-(CoP/Co_2P)@SC in Fig. 2a verifies CoP_x species is emerged and no $CoPO_x$ observed. The above results indicate $CoPO_x$ has a low content in catalyst [35]. In Co 2p spectrum of CoO_x@SC, peaks at 778.7 eV (Co $2p_{3/2}$) and 795.7 eV (Co $2p_{1/2}$) are attributed to metallic Co^0. Peaks at 780.0 eV (Co $2p_{3/2}$) and 793.8 eV (Co $2p_{1/2}$) are assigned to Co^{2+}. The peak located at 782.2 eV corresponds to Co^{3+}. The two peaks at 786.7 eV and 802.3 eV are indexed to satellite peaks (Fig. 3c) [42,43]. Furthermore, in the Co 2p spectrum of Co@SC, the BEs at 778.5 eV and 796.7 eV are assigned to Co $2p_{3/2}$ and Co $2p_{1/2}$ of Co 2p, respectively. These results provide the evidences for the generation of Co^0. Additionally, peaks at 780.7 eV (Co $2p_{3/2}$) and 793.9 eV (Co $2p_{1/2}$) are observed for Co 2p in Co@SC, representing the existence of Co^{2+}. The BEs of 785.1 eV and 803.1 eV are belongs to satellite peaks (Fig. 3d) [42,44]. In a nutshell, the BEs of Co $2p_{3/2}$ has a positive shift and P $2p_{3/2}$ has a negative shift compared with the BEs of metallic Co (778.1 eV) and elemental phosphorus (130.0 eV), respectively [45]. The inverse shifts of BEs demonstrate that Co and P in O-(CoP/Co_2P)@SC have a partial positive charge (δ^+) and negative charge (δ^-), respectively (Figs. 2b, 3b). Additionally, the charge transfer exists in O-(CoP/Co_2P)@SC from the charge density distribution map calculated by DFT (Fig. 3e, f). The introduction of O and P elements into catalyst manipulates the d-band centers of TMPs, boosts charge transfer, optimizes the adsorption of reactant molecules and thus enhances the activity towards catalytic reaction [46–48]. In O 1 s spectrum of O-(CoP/Co_2P)@SC, peaks at 531.7 eV and 532.7 eV are belongs to −OH and surface-adsorbed water, respectively (Fig. 3g). And the O 1 s peaks of CoO_x@SC are identified as O−Co (529.8 eV), −OH (531.3 eV), and adsorbed water (532.7 eV), respectively (Fig. 3h) [49,50]. The XPS spectra of Co-P@SC without oxidation treatment were also conducted to further analyze the chemical valence in catalyst. The elements of P, Co, N, C and Si in Co-P@SC are observed (Fig. S2a). In the XPS spectrum of P 2p in Co-P@SC, peaks at 129.8 (P $2p_{3/2}$) and 130.8 eV (P $2p_{1/2}$) are ascribed to P-Co. The peak located at 133.9 eV is attributed to the P species with high valence state formed by the surface oxidation of Co_xP [45] (Fig. S2b). In the Co 2p spectrum of Co-P@SC, the peak at 778.6 eV ($2p_{3/2}$) corresponds to Co^0. Peaks at 781.7 eV ($2p_{3/2}$) and 797.5 eV ($2p_{1/2}$) are attributed to Co^{2+}. The Co species in CoP are detected in the position of 793.7 eV ($2p_{1/2}$) [35,41]. Peaks at 786.3 eV ($2p_{3/2}$) and 803.2 eV ($2p_{1/2}$) are corresponding to satellite peaks (Fig. S2c). Additionally, the C 1 s spectra of various catalysts are deconvoluted into three peaks, namely, C−C (284.8 eV), C═N (285.8 eV) and O−C═O (288.8 eV) (Fig. S2d-g) [51,52]. N and Si elements are also distinguished by XPS technology (Fig. S2h, S2i). The other detailed information is shown in Table S1. The intensity ratio of I_D/I_G derived from Raman spectroscopy is calculated to investigate the existence form of carbon. The peaks near 1346, and 1584 cm^{-1} are indexed to the two types bands of carbon (D, G) for Co@SC, CoO_x@SC, Co-P@SC, O-(CoP/Co_2P)@SC, respectively. The values of I_D/I_G are calculated as 0.73, 0.92, 0.96, 0.86 and the results illustrate a large percentage of graphite carbon in Co@SC, CoO_x@SC, Co-P@SC, O-(CoP/Co_2P)@SC (Fig. 3i, S3).

3.2. Evaluation on catalytic kinetics

Some experiments are dissected to appraise the catalytic performance of NH_3BH_3 hydrolysis. The Co contents of Co@SC-600, Co@SC, Co@SC-800, CoO_x@SC-600, CoO_x@SC, CoO_x@SC-800, O-(CoP/Co_2P)@SC-600, O-(CoP/Co_2P)@SC and O-(CoP/Co_2P)@SC-800 are calculated as 25.15%, 25.63%, 33.43%, 29.63%, 28.67%, 35.92%, 24.03%, 21.8% and 27.46% by ICP-OES (Table S2). Fig. 4a and Fig. S4a-S4f are the curves of hydrogen generation of all catalysts during NH_3BH_3 hydrolysis. The corresponding *TOFs* of various catalysts are calculated and exhibited in Fig. 4b and Table S2. From the above catalytic activity (*TOF*, min^{-1}), O-(CoP/Co_2P)@SC manifests obvious improvement in catalytic activity (*TOF*=35 min^{-1}) due to the construction of dual-active sites via O modified CoP/Co_2P heterostructure. The catalyst synthesized without SiO_2 under similar procedure with O-(CoP/Co_2P)@SC was proceeded. The curve of hydrogen generation without SiO_2 in Fig. S5 conveys a poor catalytic activity than the optimal catalyst. The results clarify that SiO_2 as a structural cocatalyst contributes to the immobilization of active sites and accelerates the catalytic performance. Considering the resource consumption, it is dispensable to further investigate the catalytic stability. Noteworthily, CoO_x@SC has advantage on catalytic activity over Co-P@SC obtained directly through *LPiS* without any oxidation treatment during NH_3BH_3 hydrolysis due to the mixed composition of Co and Co_3O_4 in CoO_x@SC. Additionally, the effect of catalysts treated at different oxidation temperatures or oxidation

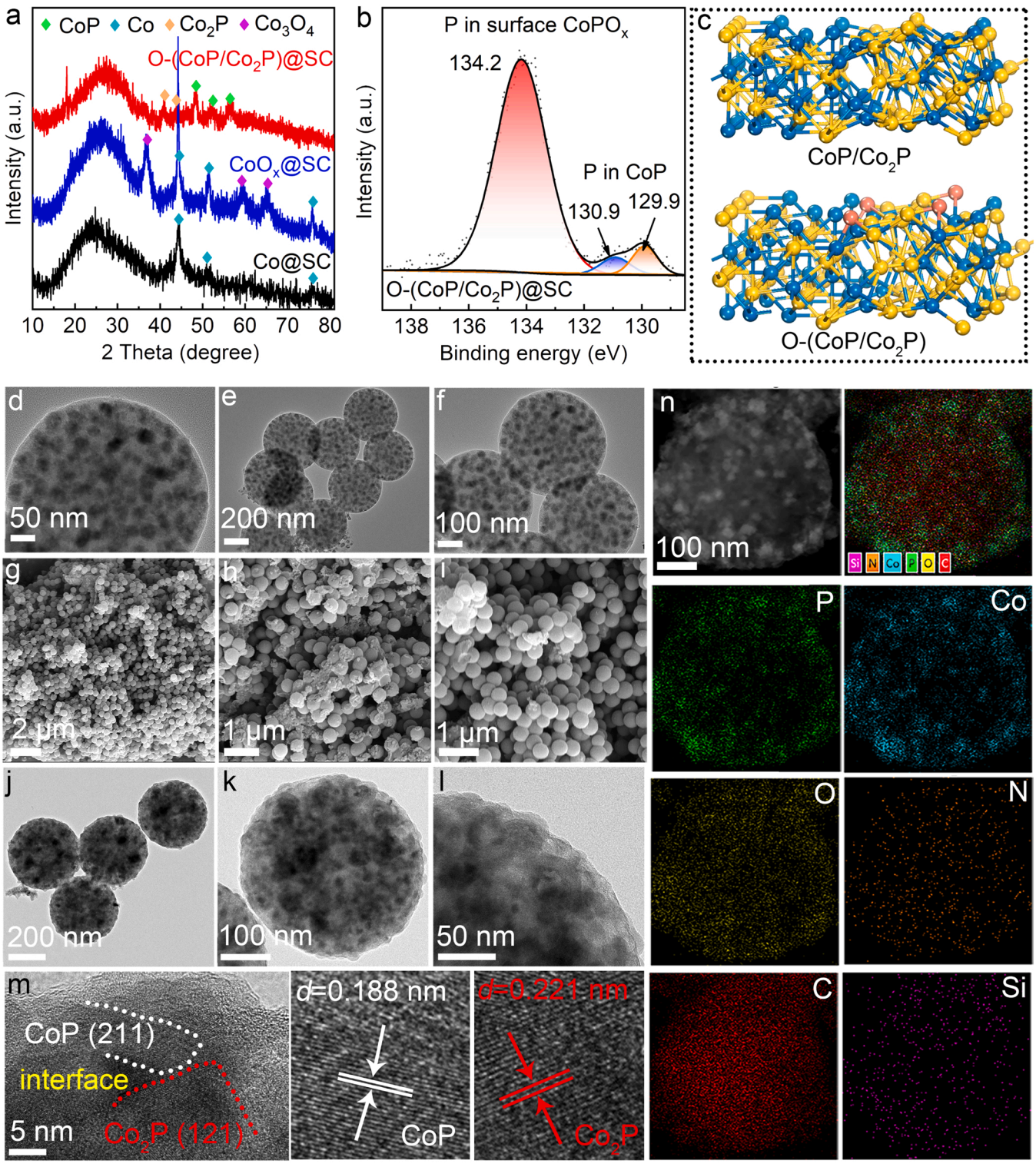

Fig. 2. (a) XRD patterns of various catalyst. (b) High resolution XPS spectra of P 2p. (c) Structural models of CoP/Co_2P and O-(CoP/Co_2P). TEM images of (d-f) CoO_x@SC, (g-i) SEM images of O-(CoP/Co_2P)@SC. (j-m) TEM and HRTEM images O-(CoP/Co_2P)@SC. (n) HAADF-STEM and corresponding EDX-STEM elemental mapping images of O-(CoP/Co_2P)@SC.

times on the catalytic activity is studied (Fig. S6a, S6b). The curves of hydrogen generation under temperature-dependent and time-dependent treatments uncover that the increase of the temperature or time has an enhancement in the catalytic activity. Moreover, the XPS spectra of the above-prepared catalysts are donated to substantiate the contents of surface O elements in catalysts. The results expound that the contents of surface O element in catalysts have an increase with the increase in different oxidation temperatures or oxidation times (Table S3). In a nutshell, the effect of the contents of surface O element in optimal catalyst on the catalytic activity is contemplated and the results verify that it exerts a tremendous fascination to ignite the catalytic activity via regulating the O contents in catalysts. Subsequently, the effect of different P-inducing temperatures or times of optimal catalyst on the catalytic activity is also surveyed. From the results in Fig. S6c and S6d,

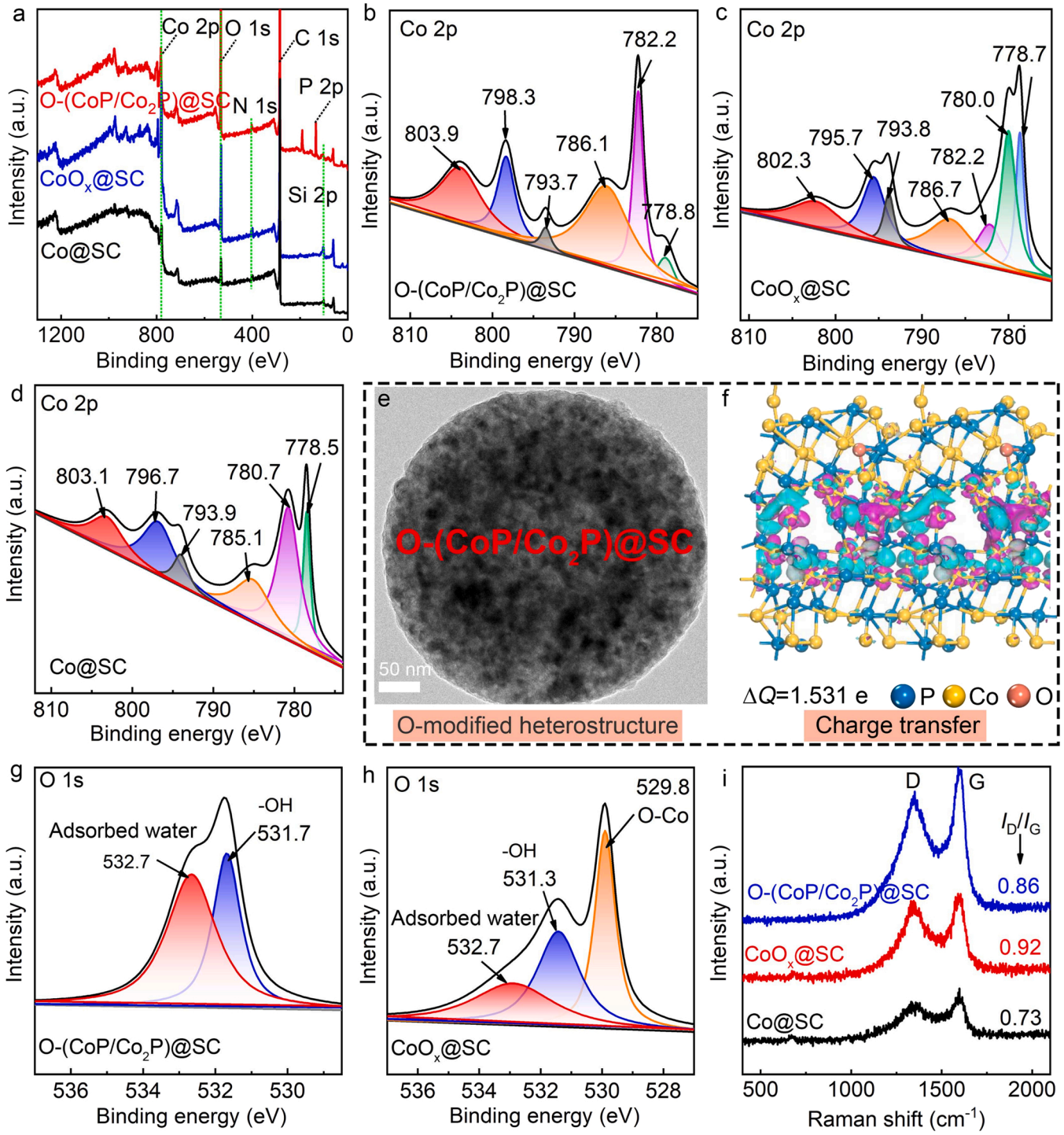

Fig. 3. (a) Survey spectra in various catalyst. XPS spectra of (b-d) Co 2p in various catalyst. (e, f) The structure of O-modified heterostructure and charge transfer diagram of O-(CoP/Co_2P)@SC. XPS spectra of (g, h) O 1 s in various catalyst. (i) Raman spectra of Co@SC, CoO_x@SC, O-(CoP/Co_2P)@SC catalyst.

the catalyst treated at 300 ℃ for 2 h presents the optimal catalytic activity. To reveal the overall effect of heterostructure on the activation energy in NH_3BH_3 hydrolysis, hydrogen generations at different temperatures are enforced in the range of 298–313 K (Fig. 4c, S7a). The *TOF* of O-(CoP/Co_2P)@SC significantly increases from 19.2 min^{-1} at 298 K to 59 min^{-1} at 313 K. From the Eq. S2, the E_a of 57.0 kJ mol^{-1} is attained (Fig. 4c). Illustratively, the comparisons of *TOFs* and E_a in catalysts from other literature are listed in Table S4.

Hydrogen generations of O-(CoP/Co_2P)@SC at different NH_3BH_3 concentrations are researched (Fig. S7b). These results distinctly demonstrate that the catalyst is suitable for different concentration of reactants, and as a symbolic evolution holds the ability to assess the stability after long-term using of the catalyst. A zero-order reaction is broached in this reaction from the changing curves of NH_3BH_3 concentration with reaction time in Fig. 4d. For the mass-dependent experiments of catalyst, the catalytic activity increase with the increase in the mass concentration of O-(CoP/Co_2P)@SC (Fig. S7c). The stability of nano-catalyst is a vital issue in the process of realizing the high efficiency of chemical production, energy catalysis and the realization of dual carbon goals. The catalytic activity of O-(CoP/Co_2P)@SC has no

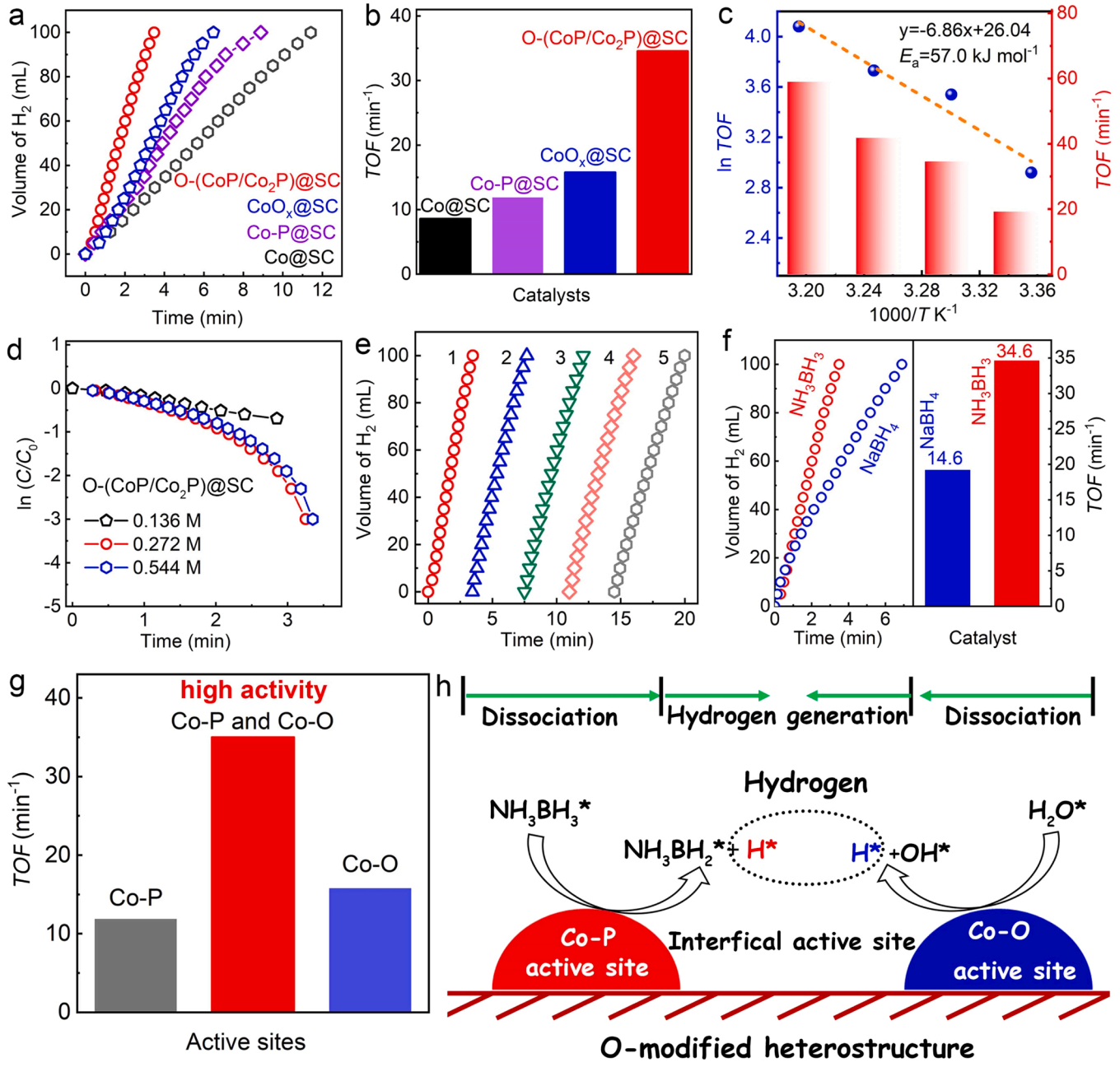

Fig. 4. (a) The curves of hydrogen generation of various catalysts. (b) Corresponding catalytic activity (*TOF*, min^{-1}). (c) The Arrhenius plot and catalytic activity (*TOF*, min^{-1}). (d) Curves of concentration changes vs time; *C*: real-time concentration; C_0: initial concentration. (e) Stability test of O-(CoP/Co_2P)@SC. (f) Hydrogen generation of O-(CoP/Co_2P)@SC for borohydride (NH_3BH_3 and $NaBH_4$) and corresponding *TOF*. (g) The comparison of *TOFs* for various catalysts over different active sites. (h) Reaction mechanism for NH_3BH_3 hydrolysis over O-(CoP/Co_2P)@SC.

tempestuous decline even after being used five cycles (Fig. 4e). Noteworthily, SiO_2 as a structural cocatalyst promotes the stability of active component in catalyst and improves the cyclic catalytic stability during hydrolysis process. $NaBH_4$ as another chemical hydrogen storage material, the catalytic activity is also carried out under similar conditions to expose the universality. A *TOF* of 19.2 min^{-1} is achieved at 303 K (Fig. 4f). The decreasing catalytic activity is emerged for $NaBH_4$ compared with NH_3BH_3 (35 min^{-1}). The reason is that the discrepant catalytic mechanism between $NaBH_4$ and NH_3BH_3 hydrolysis caused by their different molecular geometry. A comparison of catalytic activity for various catalysts over different active sites is made and corresponding results present in Fig. 4g. The construction of dual-active sites consisting of Co-O and Co-P in targeted catalyst holds the optimal activity during hydrogen generation. Fig. 4h is the conceivable catalytic mechanism of O-(CoP/Co_2P)@SC during NH_3BH_3 hydrolysis, namely, the active sites of Co-O and Co-P in O-(CoP/Co_2P)@SC activate H_2O and NH_3BH_3, respectively.

Series characterization analyses of used O-(CoP/Co_2P)@SC are also studied (Fig. S8). The phase composition of O-(CoP/Co_2P)@SC after reaction or not has no obvious changes (Fig. S8a). As anticipated, XPS analyses of the used O-(CoP/Co_2P)@SC reveal the existence of P, Co, O, N, C, Si elements with an analogical elemental valence towards to the fresh catalyst (Fig. S8b-S8h). Additionally, the elemental environment of optimal catalyst is uniformly distributed after hydrolysis reaction (Fig. S8i). The above-mentioned results demonstrate the excellent structure stability of the corresponding catalyst during catalytic system.

3.3. Insights into catalytic mechanism

DFT calculations are executed to elucidate the role of O modification in CoP/Co_2P heterostructure for NH_3BH_3 dissociation (corresponding calculation models simplified to O-CoP, O-Co_2P, CoP/Co_2P, O-(CoP/Co_2P)). The optimized structure models are presented in Fig. 5a. The adsorption energies (E_{ad}) of NH_3BH_3/H_2O on the surfaces of O-CoP, O-Co_2P, CoP/Co_2P, and O-(CoP/Co_2P) are calculated as − 0.753/− 0.418 eV, − 0.483/− 0.766 eV, − 1.457/− 1.395 eV, and − 1.751/− 1.658 eV, respectively (Fig. 5b, c). The relatively low adsorption energy means the stronger potential to preferentially adsorb the reactant molecules on the active sites and a higher concentration of reaction species on the surface of catalyst. By comparing the adsorption energies of NH_3BH_3 and H_2O molecules on various surfaces, the reactant molecules preferentially adsorb on those active sites on the surface of O-(CoP/Co_2P). The suitable adsorption energies of reactant molecules on the surface of catalyst guarantee the reaction with sufficient surface species and expedite the proceed of the whole catalytic reaction. The bond lengths of corresponding bond in reaction molecules are an important factor for the formation of the final product. Based on this, the B-H bond length in NH_3BH_3 and O-H bond length in H_2O are calculated by DFT and the values conveys as 0.994 and 1.105 Å, respectively (Fig. S9a, S9b). The B-H bond lengths in NH_3BH_3 adsorbed on the surfaces of O-CoP, O-Co_2P, CoP/Co_2P, and O-(CoP/Co_2P) are calculated as 1.165, 1.060, 1.253, and 1.291 Å, respectively (Fig. 5d). These results confirm that B-H bond in NH_3BH_3 has an obvious weak bond energy on the surface of O-(CoP/Co_2P). Coincidentally, the corresponding O-H bond lengths in H_2O on O-CoP, O-Co_2P, CoP/Co_2P, and O-(CoP/Co_2P) are calculated as 1.102, 1.187, 1.224, and 1.248 Å, respectively (Fig. 5e). Results also confirm a weak bond energy of O-H bond in H_2O molecule on the surface of O-(CoP/Co_2P). The weakening of B–H (O-H) bond energies in NH_3BH_3 (H_2O) molecule after adsorbing on the surface of O-(CoP/Co_2P) is conducive to the release of H radical [53]. Sequentially, the O modification strategy in CoP/Co_2P heterostructure dramatically weakens the bonding strength of the reaction species and effectively boosts the hydrogen generation of NH_3BH_3.

Average Bader charge analysis was calculated through DFT to further demonstrate the charge transfer from Co to P element in CoP/Co_2P and O-(CoP/Co_2P). Additionally, the enhanced charge transfer (ΔQ=1.531 e) after introducing O element reveals that O modulation accelerates the electronic transfer (Fig. 6a, b). The results have a consistent with the XPS results. The Gibbs free energies and corresponding transition states for NH_3BH_3 and H_2O dissociation on various surfaces of catalysts are calculated by DFT simulation (Figs. 6c, d). The reaction activation barrier (ΔE^*) obtained from the value of Gibbs free energy is used to confirm the catalytic kinetics of catalysts. The ΔE^* of the dissociation of NH_3BH_3 molecule on O-(CoP/Co_2P) (ΔE^*=0.535 eV) is lower than that on the surfaces of O-CoP (ΔE^*=0.910 eV), O-Co_2P (ΔE^*=1.278 eV), and

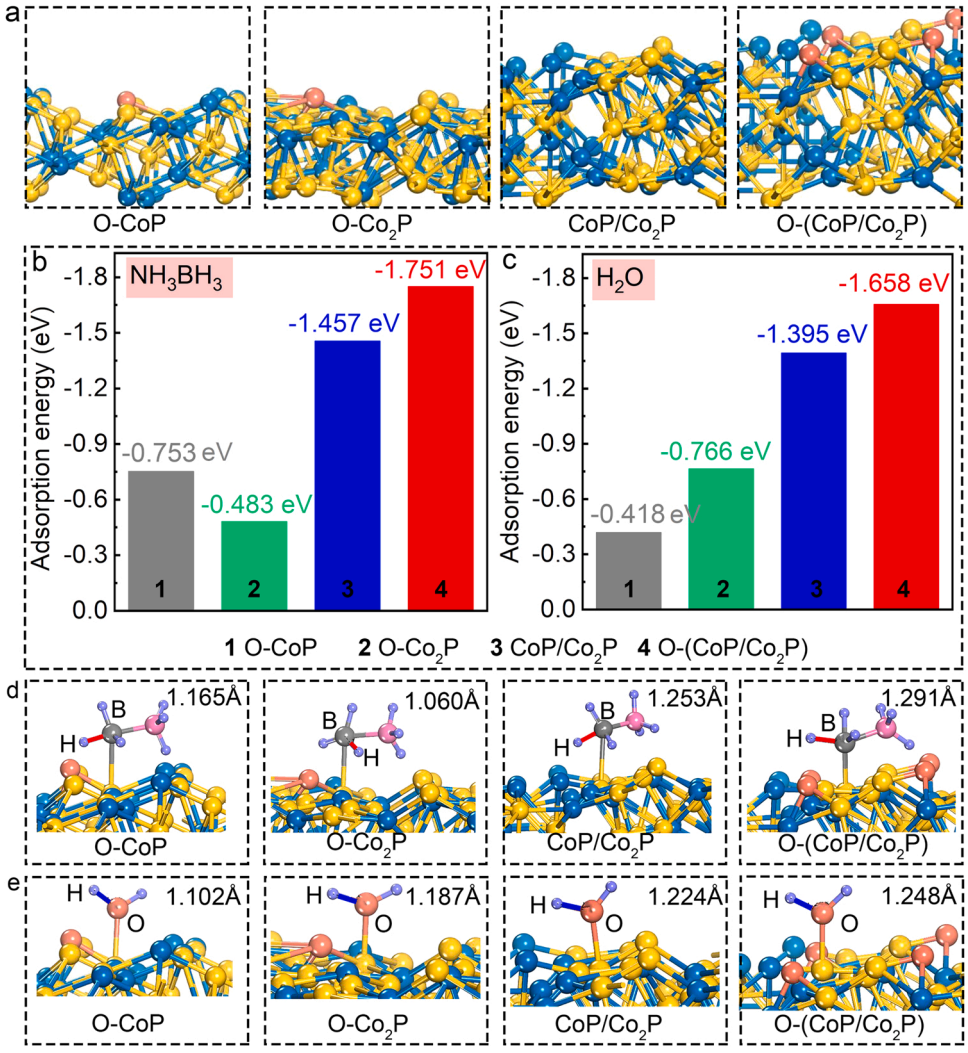

Fig. 5. (a) Optimized atomic models of various catalysts structure. (b, c) Adsorption energies of NH_3BH_3 and H_2O molecules adsorbed on various surfaces of structures. (d, e) B-H, O-H bond lengths in NH_3BH_3 and H_2O molecules on the surfaces of various catalysts.

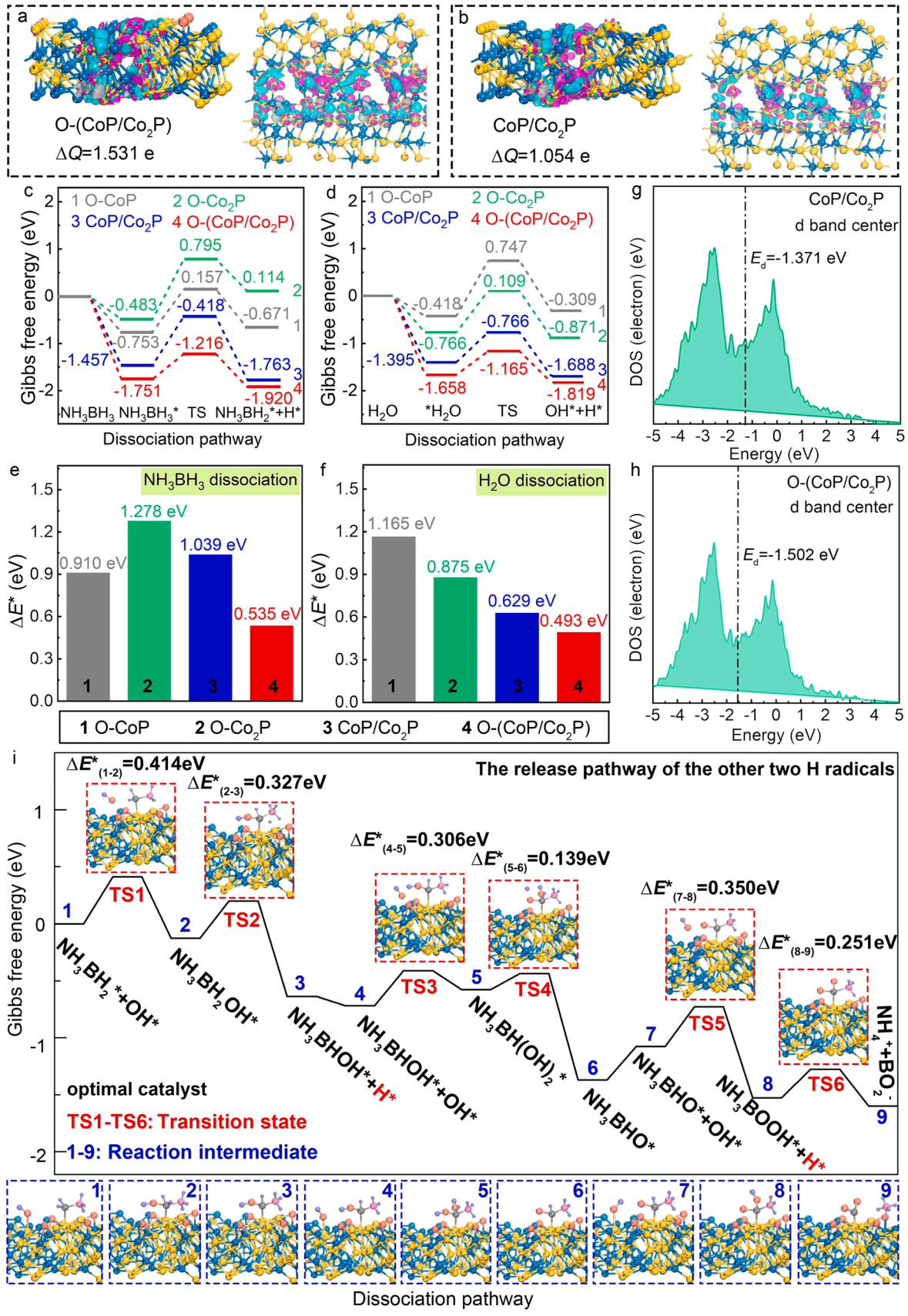

Fig. 6. (a, b) Charge density distribution map of CoP/Co_2P, O-(CoP/Co_2P). (c, d) Gibbs free energies and corresponding transition states for NH_3BH_3 and H_2O dissociation on various surfaces of catalysts. (e, f) The ΔE^* of NH_3BH_3 and H_2O dissociation on various surfaces of catalysts derived from Gibbs free energy. (g, h) d-band center of the CoP/Co_2P, O-(CoP/Co_2P). (i) The Gibbs free energies and corresponding transition states for the release of the other two radicals on the surface of O-(CoP/Co_2P).

CoP/Co_2P (ΔE^*=1.039 eV) (Fig. 6e). From above-mentioned results, O-(CoP/Co_2P) presents lowest ΔE^* value and O-CoP is a powerful contender compared with O-Co_2P in the process of NH_3BH_3 dissociation. Analogously, the ΔE^* of the dissociation of H_2O molecule on O-(CoP/Co_2P) (ΔE^*=0.493 eV) is lower than that on the surfaces of O-CoP (ΔE^*=1.165 eV), O-Co_2P (ΔE^*=0.875 eV), and CoP/Co_2P (ΔE^*=0.629 eV) (Fig. 6f). Similarly, O-(CoP/Co_2P) has the lowest ΔE^* value in H_2O dissociation and O-Co_2P is easy to activate H_2O molecule compared with O-CoP. The dissociation of NH_3BH_3 molecule on the surface of O-(CoP/Co_2P) (ΔE^*=0.535 eV) need to overcome a higher ΔE^* than that of H_2O molecule (ΔE^*=0.493 eV). The results confirm that the construction of the interfacial active sites consisting of Co-O and Co-P significantly decreases the ΔE^* of the dissociation of H_2O molecule, thus expediting the catalytic activity during the process of hydrogen generation. Illustratively, O-CoP or O-Co_2P only has the ability to activate one molecule (NH_3BH_3 or H_2O). Distinctively, O-(CoP/Co_2P) as the optimal catalyst has the coexistence of active Co elements nearby Co-P and Co-O, resulting in the ability to simultaneously activate NH_3BH_3 and H_2O molecules. The active sites in the optimal O-(CoP/Co_2P) are denoted as Co1 (active Co element nearby Co-P) and Co2 (active Co element nearby Co-O) sites, respectively (Co1 activate NH_3BH_3, Co2 activate H_2O). The lower apparent ΔE^* leads to a higher catalytic activity of O-(CoP/Co_2P) compared with the other control catalysts during NH_3BH_3 hydrolysis because of the coexistence of Co1 and Co2 dual-active sites. Additionally, the shift of the d-band center (E_d) away from the Fermi energy (E_f) level leads to a decreasing adsorption energy of intermediates on the surfaces of catalysts. The values of E_d of CoP/Co_2P and O-(CoP/Co_2P) relative to E_f are presented as − 1.371 eV and − 1.502 eV, respectively (Fig. 6g, h). The results corroborate that O modification strategy makes intermediates possess a small adsorption strength on the surface of O-(CoP/Co_2P)@SC and is beneficial to the catalytic activity. This is consistent with the d-band center theory [54]. Through experimental-theoretical results, a plausible dissociation-interaction mechanism for the hydrolysis of NH_3BH_3 is proposed as follows Eq. 3,

Special pathway:

$$NH_3BH_3+2\ [Co1]^*\rightarrow NH_3BH_2\text{-}[Co1]^*+H\text{-}[Co1]^* \quad (3-1)$$

$$H_2O+2\ [Co2]^*\rightarrow H\text{-}[Co2]^*+OH\text{-}[Co2]^* \quad (3-2)$$

$$H\text{-}[Co1]^*+H\text{-}[Co2]^*\rightarrow H_2+[Co1]^*+[Co2]^* \quad (3-3)$$

$$NH_3BH_2\text{-}[Co1]^*+OH\text{-}[Co2]^*\rightarrow NH_3BH_2OH\text{-}[Co1]^*+[Co2]^* \quad (3-4)$$

$$NH_3BH_2OH\text{-}[Co1]^*+[Co1]^*\rightarrow NH_3BHOH\text{-}[Co1]^*+H\text{-}[Co1]^* \quad (3-5)$$

$$H\text{-}[Co1]^*+H\text{-}[Co2]^*\rightarrow H_2+[Co1]^*+[Co2]^* \quad (3-6)$$

$$NH_3BHOH\text{-}[Co1]^*+OH\text{-}[Co2]^*\rightarrow NH_3BH(OH)_2\text{-}[Co1]^*+[Co2]^* \quad (3-7)$$

$$NH_3BH(OH)_2\text{-}[Co1]^*\rightarrow NH_3BHO\text{-}[Co1]^*+H_2O \quad (3-8)$$

$$NH_3BHO\text{-}[Co1]^*+[Co1]^*+OH\text{-}[Co2]^*\rightarrow NH_3BOOH\text{-}[Co1]^*+H\text{-}[Co1]^*+[Co2]^* \quad (3-9)$$

$$H\text{-}[Co1]^*+H\text{-}[Co2]^*\rightarrow H_2+[Co1]^*+[Co2]^* \quad (3-10)$$

$$NH_3BOOH\text{-}[Co1]^*\rightarrow NH_4^++BO_2^-+[Co1]^* \quad (3-11)$$

Firstly, NH_3BH_3, H_2O molecules and O-(CoP/Co_2P)@SC catalyst manifest in independent states, respectively. Subsequently, the adsorption and dissociation of the reactant molecules occur on the surface of the catalyst. From the ΔE^* values of the dissociation of NH_3BH_3 and H_2O molecules on the surface of O-(CoP/Co_2P), the Co1 activate NH_3BH_3 (named NH_3BH_3-[Co1]*) and Co2 activate H_2O (named H_2O-[Co2]*), respectively. Then the B-H bond in NH_3BH_3-[Co1]* breaks to form NH_3BH_2-[Co1]* and H-[Co1]*. The O-H bond in H_2O-[Co2]* breaks to form OH-[Co2]* and H-[Co2]*. Subsequently, H-[Co1]* combines with H-[Co2]* generates a H_2 molecule. The remaining OH-[Co2]* combines with NH_3BH_2-[Co1]* and forms NH_3BH_2OH*. Finally, NH_3BH_2OH* becomes the beginning point for further reaction and generates the other two H_2 molecules (Fig. S10) [12,55]. Additionally, the Gibbs free energies and corresponding transition states for the pathway from (3−4) to (3−11) (the release of the other two H radicals) on the optimal catalyst are calculated to analyze the whole reaction process. The ΔE^* values of the various reaction intermediates on the surface of O-(CoP/Co_2P)@SC are calculated as 0.414 eV, 0.327 eV, 0.306 eV, 0.139 eV, 0.350 eV, and 0.251 eV (Fig. 6i). The above-mentioned results confirm that the first bond-breakings of O-H and B-H in H_2O and NH_3BH_3 molecules is the rate-determining step during the whole reaction due to the higher ΔE^* compared with the other pathways. These analyses propose that the refined alteration of active sites (Co1 and Co2) via O modification on CoP/Co_2P@carbon hetero-structural catalyst effectively triggers the efficient hydrolysis of NH_3BH_3.

4. Conclusions

In conclusion, the refined alteration of active sites via O modification on CoP/Co_2P heterostructure is rationally performed to trigger the catalytic activity of catalyst toward NH_3BH_3 hydrolysis. The O-(CoP/Co_2P)@SC catalyst exhibits efficient catalytic activity (*TOF* of 35 min^{-1}) in neutral environment. Moreover, the optimal catalyst delivers excellent catalytic ability without obvious loss even after five cycles. The superior catalytic activity is contributed to the modulation of coordination environment and electronic structure of Co active sites through the O modification on CoP/Co_2P. Confirmed by experimental results and DFT simulations, the refined alteration of active sites via O modification strategy on CoP/Co_2P heterostructure dramatically reduces the dissociation energies of NH_3BH_3 and H_2O molecules on the surface of catalyst, consequently optimizing the reaction kinetics of catalytic hydrolysis. This O modification concept holds new insights into optimizing nano-catalysts via hetero-structural phase and non-metallic atomic regulation strategies.

CRediT authorship contribution statement

Huanhuan Zhang: Investigation, Visualization, Writing – original draft, Writing – review & editing, Formal analysis. **Yanyan Liu:** Visualization, Formal analysis, Supervision, the supporting of contribution. **Limin Zhou:** Writing – review & editing, Formal analysis, the supporting of contribution. **Huijuan Wei:** Writing – review, Formal analysis, the supporting of contribution. **Hao Wen:** Writing – review & editing, Formal analysis, the supporting of contribution. **Zhenggang Wang:** Writing – review & editing, Formal analysis, the supporting of contribution. **Xinzheng Yue:** Writing – review & editing, Formal analysis, the supporting of contribution. **Xianli Wu:** Writing – review & editing, Formal analysis, the supporting of contribution. **Yulong Zhang:** Writing – review & editing, Formal analysis, the supporting of contribution. **Baozhong Liu:** Visualization, Formal analysis, Supervision, the supporting of contribution. **Yanping Fan:** Project administration, Visualization, Formal analysis, Supervision, the supporting of contribution. **Huaqiang Cao:** Writing – review & editing, Formal analysis, the supporting of contribution. **Jianchun Jiang:** Writing – review & editing, Formal analysis, the supporting of contribution. **Baojun Li:** Funding acquisition, Formal analysis, Supervision, Conceptualization, the lead of contribution.

Declaration of Competing Interest

The authors declare that they have no known competing financial interests or personal relationships that could have appeared to influence the work reported in this paper.

Data Availability

The authors do not have permission to share data.

Acknowledgments

Financial supports from the National Natural Science Foundation of China (no. 22075254, no. U22A20120, no. 52071135, no. 51871090 and no. U1804135), the Natural Science Foundation of Hebei Province for Innovation Groups Program (no. C2022203003) and Fundamental Research Funds for the Universities of Henan Province (no. NSFRF220201).

Supporting information

The details of the synthesis, characterizations, and catalytic measurements, and more SEM and TEM images as well as the evaluation of catalytic performance.

Appendix A. Supporting information

Supplementary data associated with this article can be found in the online version at doi:10.1016/j.apcatb.2022.122324.

References

[1] D.-X. Liu, Y.-T. Zhou, Y.-F. Zhu, Z.-Y. Chen, J.-M. Yan, Q. Jiang, Tri-metallic AuPdIr nanoalloy towards efficient hydrogen generation from formic acid, Appl. Catal. B Environ. 309 (2022), 121228.
[2] D. Bu, D. Bu, W. Chen, C. Huang, L. Li, H. Lei, S. Huang, Metal-organic frameworks with mixed-anion secondary building units as efficient photocatalysts for hydrogen generation, J. Catal. 407 (2022) 10–18.
[3] C. Wang, Y. Ren, J. Zhao, S. Sun, X. Du, M. Wang, G. Ma, H. Yu, L. Li, X. Yu, X. Zhang, Z. Lu, X. Yang, Oxygen vacancy-attired dual-active-sites Cu/$Cu_{0.76}Co_{2.24}O_4$ drives electron transfer for efficient ammonia borane dehydrogenation, Appl. Catal. B Environ. 314 (2022), 121494.
[4] R.-T. Gao, X. Guo, S. Liu, X. Zhang, X. Liu, Y. Su, L. Wang, Ultrastable and high-performance seawater-based photoelectrolysis system for solar hydrogen generation, Appl. Catal. B Environ. 304 (2022), 120883.
[5] D. Wei, R. Sang, P. Sponholz, H. Junge, M. Beller, Reversible hydrogenation of carbon dioxide to formic acid using a Mn-pincer complex in the presence of lysine, Nat. Energy 7 (2022) 438–447.
[6] Y. Feng, Y. Li, Q. Liao, W. Zhang, Z. Huang, X. Chen, Y. Shao, H. Dong, Q. Liu, H. Li, Modulation the electronic structure of hollow structured CuO-$NiCo_2O_4$ nanosphere for enhanced catalytic activity towards methanolysis of ammonia borane, Fuel 332 (2023), 126045.
[7] Y. Liu, G. Han, X. Zhang, C. Xing, C. Du, H. Cao, B. Li, Co-Co_3O_4@carbon core-shells derived from metal-organic framework nanocrystals as efficient hydrogen evolution catalysts, Nano Res 10 (2017) 3035–3048.
[8] Z. Zhang, S. Zhang, Q. Yao, G. Feng, M. Zhu, Z.-H. Lu, Metal-organic framework immobilized RhNi alloy nanoparticles for complete H_2 evolution from hydrazine borane and hydrous hydrazine, Inorg. Chem. Front. 5 (2018) 370–377.
[9] A. Zhang, J. Xia, Q. Yao, Z.-H. Lu, Pd–WO_x heterostructures immobilized by MOFs-derived carbon cage for formic acid dehydrogenation, Appl. Catal. B Environ. 309 (2022), 121278.
[10] J. Wang, Y. Yu, W. Xu, H. Yu, W. Zhang, H. Huang, G.-R. Zhang, D. Mei, Covalent triazine framework encapsulated Pd nanoclusters for efficient hydrogen production via ammonia borane hydrolysis, J. Catal. 411 (2022) 72–83.
[11] Y. Liu, H. Wen, D. Zhou, X. Huang, X. Wu, J. Jiang, X. Guo, B. Li, Tuning surface d charge of Ni-Ru alloys for unprecedented catalytic activity towards hydrogen generation from ammonia borane hydrolysis, Appl. Catal. B Environ. 291 (2021), 120094.
[12] R. Shen, Y. Liu, H. Wen, T. Liu, Z. Peng, X. Wu, X. Ge, S. Mehdi, H. Cao, E. Liang, J. Jiang, B. Li, Engineering V_O-Ti ensemble to boost the activity of Ru towards water dissociation for catalytic hydrogen generation, Appl. Catal. B Environ. 306 (2022), 121100.
[13] S. Gong, W. Wang, C. Zhang, M. Zhu, R. Lu, J. Ye, H. Yang, C. Wu, J. Liu, D. Rao, S. Shao, X. Lv, Tuning the metal electronic structure of anchored cobalt phthalocyanine via dual-regulator for efficient CO_2 electroreduction and Zn-CO_2 batteries, Adv. Funct. Mater. 32 (2022) 2110649.
[14] R. Ding, D. Li, Y. Li, J. Yu, M. Jia, J. Xu, Bimetallic PdAu nanoparticles in amine-containing metal-organic framework UiO-66 for catalytic dehydrogenation of formic acid, ACS Appl. Nano Mater. 4 (2021) 4632–4641.
[15] Z. Chen, G. Zhang, Y. Wen, N. Chen, W. Chen, T. Regier, J. Dynes, Y. Zheng, S. Sun, Atomically dispersed Fe-Co bimetallic catalysts for the promoted electroreduction of carbon dioxide, Nano-Micro Lett. 14 (2022) 25.
[16] Y. Ge, X. Qin, A. Li, Y. Deng, L. Lin, M. Zhang, Q. Yu, S. Li, M. Peng, Y. Xu, X. Zhao, M. Xu, W. Zhou, S. Yao, D. Ma, Maximizing the synergistic effect of CoNi catalyst on α-MoC for robust hydrogen production, J. Am. Chem. Soc. 143 (2021) 628–633.
[17] L. Wang, J. Fan, Y. Liu, M. Chen, Y. Lin, H. Bi, B. Liu, N. Shi, D. Xu, J. Bao, M. Han, Phase-modulation of iron/nickel phosphides nanocrystals "armored" with porous P-doped carbon and anchored on P-doped graphene nanohybrids for enhanced overall water splitting, Adv. Funct. Mater. 31 (2021) 2010912.
[18] L. Zhou, P. Jiao, L. Fang, L. Liu, Z. Hao, H. Wang, Y.-M. Kang, K. Zhang, J. Chen, Two-phase transition induced amorphous metal phosphides enabling rapid, reversible alkali-metal ion storage, ACS Nano 15 (2021) 13486–13494.
[19] Z. Chen, X. Zeng, X. Li, Z. Lv, J. Li, Y. Zhang, Strong metal phosphide–phosphate support interaction for enhanced non-noble metal catalysis, Adv. Mater. 34 (2022) 2106724.
[20] J. Mao, J. Iocozzia, J. Huang, K. Meng, Y. Lai, Z. Lin, Graphene aerogels for efficient energy storage and conversion, Energy Environ. Sci. 11 (2018) 772–799.
[21] C.-C. Hou, Q. Li, C.-J. Wang, C.-Y. Peng, Q.-Q. Chen, H.-F. Ye, W.-F. Fu, C.-M. Che, N. López, Y. Chen, Ternary Ni-Co-P nanoparticles as noble-metal-free catalysts to boost the hydrolytic dehydrogenation of ammonia-borane, Energy Environ. Sci. 10 (2017) 1770–1776.
[22] L.-M. Cao, J. Zhang, L.-W. Ding, Z.-Y. Du, C.-T. He, Metal-organic frameworks derived transition metal phosphides for electrocatalytic water splitting, J. Energy Chem. 68 (2022) 494–520.
[23] X. Xiao, C.-T. He, S. Zhao, J. Li, W. Lin, Z. Yuan, Q. Zhang, S. Wang, L. Dai, D. Yu, A general approach to cobalt-based homobimetallic phosphide ultrathin nanosheets for highly efficient oxygen evolution in alkaline media, Energy Environ. Sci. 10 (2017) 893–899.
[24] H. Guo, Q. Feng, K. Xu, J. Xu, J. Zhu, C. Zhang, T. Liu, Self-templated conversion of metallogel into heterostructured TMP@Carbon quasiaerogels boosting bifunctional electrocatalysis, Adv. Funct. Mater. 29 (2019) 1903660.
[25] H. Lu, W. Fan, Y. Huang, T. Liu, Lotus root-like porous carbon nanofiber anchored with CoP nanoparticles as all-pH hydrogen evolution electrocatalysts, Nano Res. 11 (2018) 1274–1284.
[26] H. Wang, Z. Niu, Z. Peng, X. Wu, C. Gao, S. Zhao, Y.D. Kim, H. Wu, X. Du, Z. Liu, B. Li, Engineering interface on a 3D $Co_xNi_{1-x}(OH)_2$@MoS_2 hollow heterostructure for robust electrocatalytic hydrogen evolution, ACS Appl. Mater. Interfaces 14 (2022) 9116–9125.
[27] Z. Li, M. Hu, J. Liu, W. Wang, Y. Li, W. Fan, Y. Gong, J. Yao, P. Wang, M. He, Y. Li, Mesoporous silica stabilized MOF nanoreactor for highly selective semi-hydrogenation of phenylacetylene via synergistic effect of Pd and Ru single site, Nano Res. 15 (2022) 1983–1992.
[28] S. Wang, K. Feng, D. Zhang, D. Yang, M. Xiao, C. Zhang, L. He, B. Yan, G.A. Ozin, W. Sun, Stable Cu catalysts supported by two-dimensional SiO_2 with strong metal-support interaction, Adv. Sci. 9 (2022) 2104972.
[29] T.W. van Deelen, C. Hernández Mejía, K.P. de Jong, Control of metal-support interactions in heterogeneous catalysts to enhance activity and selectivity, Nat. Catal. 2 (2019) 955–970.
[30] J. Luo, J. Wang, Y. Guo, J. Zhu, H. Jin, Z. Zhang, D. Zhang, Y. Niu, S. Hou, J. Du, D. He, Y. Xiong, L. Chen, S. Mu, Y. Huang, Metal-organic frameworks derived RuP_2 with yolk-shell structure and efficient performance for hydrogen evolution reaction in both acidic and alkaline media, Appl. Catal. B Environ. 305 (2022), 121043.
[31] J. Kim, H. Jung, S.-M. Jung, J. Hwang, D.Y. Kim, N. Lee, K.-S. Kim, H. Kwon, Y.-T. Kim, J.W. Han, J.K. Kim, Tailoring binding abilities by incorporating oxophilic transition metals on 3D nanostructured Ni arrays for accelerated alkaline hydrogen evolution reaction, J. Am. Chem. Soc. 143 (2021) 1399–1408.
[32] G. Zhou, M. Li, Y. Li, H. Dong, D. Sun, X. Liu, L. Xu, Z. Tian, Y. Tang, Regulating the electronic structure of CoP nanosheets by O incorporation for high-efficiency electrochemical overall water splitting, Adv. Funct. Mater. 30 (2019) 1905252.
[33] L. Zhang, J. Ye, Y. Tu, Q. Wang, H. Pan, L. Wu, X. Zheng, J. Zhu, Oxygen modified CoP_2 supported palladium nanoparticles as highly efficient catalyst for hydrolysis of ammonia borane, Nano Res. 15 (2021) 3034–3041.
[34] H. Zhang, Y. Fan, B. Liu, Y. Liu, S. Ashraf, X. Wu, G. Han, J. Gao, B. Li, Birdcage-type CoO_x-carbon catalyst derived from metal–organic frameworks for enhanced hydrogen generation, ACS Sustain. Chem. Eng. 7 (2019) 9782–9792.
[35] J.-X. Feng, S.-Y. Tong, Y.-X. Tong, G.-R. Li, Pt-like hydrogen evolution electrocatalysis on PANI/CoP hybrid nanowires by weakening the shackles of hydrogen ions on the surfaces of catalysts, J. Am. Chem. Soc. 140 (2018) 5118–5126.
[36] Y. Pan, K. Sun, S. Liu, X. Cao, K. Wu, W.-C. Cheong, Z. Chen, Y. Wang, Y. Li, Y. Liu, D. Wang, Q. Peng, C. Chen, Y. Li, Core-shell ZIF-8@ZIF-67-derived CoP nanoparticle-embedded N-doped carbon nanotube hollow polyhedron for efficient overall water splitting, J. Am. Chem. Soc. 140 (2018) 2610–2618.
[37] J. Bai, B. Xi, H. Mao, Y. Lin, X. Ma, J. Feng, S. Xiong, One-step construction of N,P-codoped Porous carbon sheets/CoP hybrids with enhanced lithium and potassium storage, Adv. Mater. 30 (2018) 1802310.
[38] C.-D. Si, Z.-X. Wu, J. Wang, Z.-H. Lu, X.-F. Xu, J.-S. Li, Enhanced the hydrogen evolution performance by ruthenium nanoparticles doped into cobalt phosphide nanocages, ACS Sustain. Chem. Eng. 7 (2019) 9737–9742.
[39] R. Boppella, J. Tan, W. Yang, J. Moon, Homologous CoP/NiCoP heterostructure on N-doped carbon for highly efficient and pH-universal hydrogen evolution electrocatalysis, Adv. Funct. Mater. 29 (2019) 1807976.
[40] Q. Shi, Q. Liu, Y. Zheng, Y. Dong, L. Wang, H. Liu, W. Yang, Controllable construction of bifunctional Co_xP@N,P-doped carbon electrocatalysts for rechargeable zinc-air batteries, Energy Environ. Mater. 5 (2022) 515–523.
[41] M.M. Alsabban, M.K. Eswaran, K. Peramaiah, W. Wahyudi, X. Yang, V. Ramalingam, MohamedN. Hedhili, X. Miao, U. Schwingenschlögl, L.-J. Li, V. Tung, K.-W. Huang, Unusual activity of rationally designed cobalt phosphide/

oxide heterostructure composite for hydrogen production in alkaline medium, ACS Nano 16 (2022) 3906–3916.
[42] L. Wang, Y. Liu, S. Ashraf, J. Jiang, G. Han, J. Gao, X. Wu, B. Li, Pitaya pulp structural cobalt-carbon composite for efficient hydrogen generation from borohydride hydrolysis, J. Alloy. Compd. 808 (2019), 151774.
[43] P. Dai, Y. Yao, E. Hu, D. Xu, Z. Li, C. Wang, Self-assembled ZIF-67@graphene oxide as a cobalt-based catalyst precursor with enhanced catalytic activity toward methanolysis of sodium borohydride, Appl. Surf. Sci. 546 (2021), 149128.
[44] G. Yang, S. Guan, S. Mehdi, Y. Fan, B. Liu, B. Li, Co-CoO_x supported onto TiO_2 coated with carbon as a catalyst for efficient and stable hydrogen generation from ammonia borane, Greeen Energy Environ. 6 (2021) 236–243.
[45] H. Zhang, K. Zhang, S. Ashraf, Y. Fan, S. Guan, X. Wu, Y. Liu, B. Liu, B. Li, Polar O-Co-P surface for bimolecular activation in catalytic hydrogen generation, Energy Environ. Mater. (2022), https://doi.org/10.1002/eem2.12273.
[46] Y. Liu, Z. Zhang, L. Zhang, Y. Xia, H. Wang, H. Liu, J. Yu, Manipulating the d-band centers of transition metal phosphide through dual metal doping towards robust overall water splitting, J. Mater. Chem. A 10 (2022) 22125–22134.
[47] X. Yang, C. Xing, B. Zhang, X. Liu, H. Liang, G. Luo, G. Zhang, Z. Li, S. Zhao, J. Zhang, G. Wang, Y. Qin, Direct bonding of CpCo- fragments on Pt nanoparticles and their electronic effect for alkyne semihydrogenation, ACS Catal. 12 (2022) 0849–10856.
[48] S. Mondal, S. Sarkar, D. Bagchi, T. Das, R. Das, A.K. Singh, P.K. Prasanna, C. P. Vinod, S. Chakraborty, S.C. Peter, Morphology-tuned Pt_3Ge accelerates water dissociation to industrial-standard hydrogen production over a wide pH range, Adv. Mater. 34 (2022) 2202294.
[49] H. Wu, M. Wu, B. Wang, X. Yong, Y. Liu, B. Li, B. Liu, S. Lu, Interface electron collaborative migration of Co-Co_3O_4/carbon dots: boosting the hydrolytic dehydrogenation of ammonia borane, J. Energy Chem. 48 (2020) 43–53.
[50] S. Guan, L. Zhang, H. Zhang, Y. Guo, B. Liu, H. Wen, Y. Fan, B. Li, Defect-rich Co-CoO_x-Graphene nanocatalysts for efficient hydrogen production from ammonia borane, Chem. Asian J. 15 (2020) 3087–3095.
[51] S. Guan, L. An, S. Ashraf, L. Zhang, B. Liu, Y. Fan, B. Li, Oxygen vacancy excites Co_3O_4 nanocrystals embedded into carbon nitride for accelerated hydrogen generation, Appl. Catal. B Environ. 269 (2020), 118775.
[52] H. Song, J. Yu, Z. Tang, B. Yang, S. Lu, Halogen-doped carbon dots on amorphous cobalt phosphide as robust electrocatalysts for overall water splitting, Adv. Energy Mater. 12 (2022) 2102573.
[53] D. Fan, X. Lv, J. Feng, S. Zhang, J. Bai, R. Lu, J. Liu, Cobalt nickel nanoparticles encapsulated within hexagonal boron nitride as stable, catalytic dehydrogenation nanoreactor, Int. J. Hydrog. Energy 42 (2017) 11312–11320.
[54] Y. Chen, J. Cai, P. Li, G. Zhao, G. Wang, Y. Jiang, J. Chen, S.X. Dou, H. Pan, W. Sun, Hexagonal boron nitride as a multifunctional support for engineering efficient electrocatalysts toward the oxygen reduction reaction, Nano Lett. 20 (2020) 6807–6814.
[55] H. Zhang, Y. Liu, H. Wei, C. Wang, T. Liu, X. Wu, S. Ashraf, S. Mehdi, S. Guan, Y. Fan, X. Yue, B. Liu, Y. Zhang, H. Cao, B. Li, Atomic-bridge structure in B-Co-P dual-active sites on boron nitride nanosheets for catalytic hydrogen generation, Appl. Catal. B Environ. 314 (2022), 121495.